

Geophysical Research Letters®



RESEARCH LETTER

10.1029/2025GL119875

Photosynthetic Recovery Dynamics Reveal Declining Vegetation Functional Resilience in Tropical Ecosystems

Subhrasita Behera¹ , Chan Diao^{2,3}, Sebastian Bathiany^{3,4} , Niklas Boers^{3,4}, and Debsunder Dutta¹ 

¹Department of Civil Engineering, Indian Institute of Science, Bangalore, India, ²Faculty of Geographical Science, Beijing Normal University, Beijing, China, ³Climate Center and Department of Aerospace and Geodesy, School of Engineering and Design, Technical University of Munich, Munich, Germany, ⁴Potsdam Institute for Climate Impact Research, Potsdam, Germany

Key Points:

- SIF-based recovery shows clear latitudinal gradients with fast recovery in boreal zones and persistent vulnerability in the tropics
- Long-term trends show resilience loss in Eurasian high latitudes
- Short-term trends show accelerating tropical resilience loss driven by heat, vapor pressure deficit, and soil moisture stress

Supporting Information:

Supporting Information may be found in the online version of this article.

Correspondence to:

D. Dutta,
ddutta@iisc.ac.in

Citation:

Behera, S., Diao, C., Bathiany, S., Boers, N., & Dutta, D. (2026). Photosynthetic recovery dynamics reveal declining vegetation functional resilience in tropical ecosystems. *Geophysical Research Letters*, 53, e2025GL119875. <https://doi.org/10.1029/2025GL119875>

Received 6 OCT 2025
Accepted 16 MAR 2026

Author Contributions:

Conceptualization: Subhrasita Behera, Niklas Boers, Debsunder Dutta
Data curation: Subhrasita Behera
Formal analysis: Subhrasita Behera
Funding acquisition: Debsunder Dutta
Investigation: Subhrasita Behera, Niklas Boers, Debsunder Dutta
Methodology: Subhrasita Behera, Niklas Boers, Debsunder Dutta
Project administration: Debsunder Dutta
Resources: Debsunder Dutta
Supervision: Debsunder Dutta
Validation: Subhrasita Behera
Visualization: Subhrasita Behera, Chan Diao, Debsunder Dutta
Writing – original draft: Subhrasita Behera

© 2026. The Author(s).

This is an open access article under the terms of the [Creative Commons Attribution-NonCommercial License](https://creativecommons.org/licenses/by-nc/4.0/), which permits use, distribution and reproduction in any medium, provided the original work is properly cited and is not used for commercial purposes.

Abstract Ecosystem resilience, the ability to recover from disturbances, is crucial for sustaining ecosystem health and functionality. Traditional greenness-based resilience measures often overlook early physiological stress. Here, we use solar-induced chlorophyll fluorescence (SIF), an indicator for photosynthesis, to assess global vegetation functional resilience from 2000 to 2019. Using indicators of critical slowing down, we derive recovery rates as a measure of resilience from variance and autocorrelation in SIF time series across natural vegetation. Our results reveal marked latitudinal contrasts, with faster recovery in boreal regions and persistent vulnerability in tropical and low-latitude ecosystems. Long-term trends show resilience loss in the Eurasian high latitudes, while short-term trends indicate accelerating resilience decline in 60.7% of the global tropics, driven by heat, vapor pressure deficit, and soil moisture stress. These findings highlight the need to monitor ecosystem functional resilience through physiological indicators to anticipate ecological tipping points and inform conservation and climate adaptation strategies.

Plain Language Summary Ecosystem resilience governs the stability of carbon and water cycles, yet conventional assessments based on vegetation greenness often overlook early physiological stress. By leveraging solar-induced chlorophyll fluorescence (SIF), an indicator of photosynthesis, we quantify global patterns of functional resilience over two decades. Our analyses show strong latitudinal contrasts with rapid recovery in boreal systems and widespread resilience declines across Eurasian high latitudes. In recent years, tropical ecosystems show accelerating resilience loss driven by intensifying heat, vapor pressure deficit, and soil moisture stress. This emerging global mosaic of resilience gains and losses highlights the urgency of monitoring functional resilience as a critical basis for ecosystem conservation, adaptive land management, and climate mitigation strategies.

1. Introduction

Vegetation resilience is defined as the capacity of ecosystems to withstand and recover from disturbances, maintaining their essential structure and function (Scheffer et al., 2009). It is a crucial property that governs ecosystem stability and influences the sustainability of biodiversity, carbon cycling, and other ecosystem services in the face of environmental change (Allen et al., 2010; Dakos et al., 2012). Previous studies have demonstrated that resilience varies across biomes and climatic gradients, often declining in regions experiencing intensified drought, warming, and human impacts (Pettorelli et al., 2005). Previous research has also highlighted the importance of early-warning indicators as signals of declining resilience and impending critical transitions (Boers & Rypdal, 2021; Dakos et al., 2008). These insights collectively highlight the importance of resilience assessment for anticipating ecosystem vulnerability and guiding effective management under global change. Accurate resilience assessments enable policymakers and conservationists to prioritize vulnerable regions and implement interventions aimed at maintaining ecosystem function under mounting environmental stress (Carpenter & Brock, 2011).

Resilience in ecosystems can be estimated using the theory of critical slowing down (CSD), which posits that as a system approaches a critical threshold or tipping point, its ability to recover from disturbances diminishes (Boers et al., 2022; Dakos et al., 2008; Scheffer et al., 2009; Smith et al., 2022). CSD reflects declining recovery rates, which can be detected through changes in the statistical properties of time series. Specifically, the lag-one autocorrelation (AC1) and variance are key metrics that reflect the dynamical stability of the system. AC1

Writing – review & editing:

Subhasita Behera, Chan Diao,
Sebastian Bathiany, Niklas Boers,
Debsunder Dutta

measures the correlation between consecutive observations in a time series, effectively capturing the system's “memory” of past states. Higher AC1 values indicate slower recovery and stronger persistence of disturbances (Dakos et al., 2012). Variance quantifies the magnitude of fluctuations around the system's equilibrium; as resilience weakens, variance typically increases due to greater sensitivity to environmental noise (Boers & Rypdal, 2021). Together, rising AC1 and variance serve as early-warning indicators of declining resilience and impending critical transitions (Smith et al., 2022). These metrics are derived using the framework of stochastic differential equations, often modeled as Ornstein–Uhlenbeck processes, which describe the system's response to perturbations and stochastic forcing (Dijkstra, 2013). Patterns of resilience and changes thereof can hence be monitored globally by applying these methods to high-resolution ecological data sets, including remotely sensed vegetation signals, providing crucial insights into ecosystem vulnerability and stability under changing environmental conditions.

Previous research on vegetation resilience has predominantly utilized greenness-based optical remote sensing indices, such as the Normalized Difference Vegetation Index (NDVI), Enhanced Vegetation Index (EVI), and leaf area index (LAI), which capture canopy structure (Chen et al., 2024; Forzieri et al., 2021; Smith & Boers, 2023a). Although valuable for monitoring vegetation status, these structural indices have inherent limitations. They primarily reflect canopy greenness rather than physiological function, potentially missing early signs of stress (Zarco-Tejada et al., 2013). Further, Smith and Boers (2023b) demonstrated that the reliability of resilience estimates based on optical indices critically depends on biomass density. In high-biomass ecosystems, such indices may underestimate or obscure functional declines, underscoring the limitations of these indices in capturing true ecosystem functional resilience. Additionally, other indicator such as Vegetation Optical Depth (VOD) provides a complementary functional metric sensitive to vegetation water content, offering insights into drought stress, but it still does not directly measure photosynthetic activity (Wang et al., 2021). Photosynthesis inherently couples carbon uptake with water loss through stomatal regulation, making photosynthetic activity a sensitive integrator of plant physiological status and environmental stress (Lawlor & Cornic, 2002). Capturing photosynthetic activity is essential because it reflects the core functional state of vegetation that controls both carbon assimilation and water use, key processes governing ecosystem productivity and climate feedbacks.

Solar-induced chlorophyll fluorescence (SIF) has emerged as a powerful tool for monitoring terrestrial photosynthesis and ecosystem functioning across regional to global scales (Behera & Dutta, 2024; Frankenberg et al., 2011; Sun et al., 2017). SIF represents the re-emission of light in the 650–850 nm spectral range following chlorophyll excitation by absorbed photosynthetically active radiation (APAR), providing a proxy and sensitive indicator of photosynthetic activity. As a measure of the core physiological process driving carbon assimilation and coupled water fluxes, SIF captures real-time changes in photosynthetic function before structural changes in vegetation occur. This makes SIF uniquely suited for detecting early stress responses and assessing vegetation functional resilience (Behera et al., 2025; Mohammadi et al., 2022).

Building on these recent methodological advances, in this study we use long-term global SIF data sets to quantify vegetation functional resilience across natural ecosystems. In this study, we quantify functional (engineering) resilience, defined as the rate at which photosynthetic activity returns toward equilibrium following short-term disturbances. Specifically, we apply the theory of CSD to derive key resilience metrics, such as recovery rates, from temporally continuous SIF time series, which capture vegetation photosynthetic activity at high spatial and temporal resolutions. We analyze spatial patterns and latitudinal gradients of vegetation resilience globally, and examine how resilience has shifted over time. Further, detecting shifts in short-term trends is crucial for uncovering emerging ecosystem vulnerabilities that may be obscured by long-term trend analyses (De Jong et al., 2012). Thus, additionally, we analyzed the trajectory of resilience trends over time by comparing two decades (2000–2009 and 2010–2019), focusing on how the direction and rate of change in resilience trends have evolved. Further, we investigate how resilience trends and their dynamics vary across land use land cover (LULC) types, and across major climate zones, to identify LULC and climate-specific vulnerabilities and adaptive capacities. Finally, by integrating climate and soil moisture data, we explore the environmental drivers underlying observed changes in vegetation functional resilience. This comprehensive framework constitutes the first global assessment of vegetation functional resilience based on a physiological remote sensing indicator. It provides novel insights into ecosystem stability, vulnerability to climatic stressors, and the broader implications of environmental change on terrestrial biosphere functioning.

2. Data and Methods

2.1. Vegetation and Land Use-Land Cover (LULC) Data

We utilized the global continuous solar-induced chlorophyll fluorescence (CSIF) data set, providing solar-induced fluorescence (SIF) data at a spatial resolution of 0.05° and a temporal resolution of four days spanning from 2000 to 2019 (Zhang et al., 2018). The CSIF product is generated using a neural network model trained on sparse Orbiting Carbon Observatory-2 (OCO-2) SIF observations and daily nadir bidirectional adjusted reflectance data from the Moderate Resolution Imaging Spectroradiometer (MODIS). This approach facilitates high spatial and temporal continuity, accurately capturing vegetation dynamics. The data set shows strong agreement with satellite-derived daily SIF measurements from OCO-2 and Global Ozone Monitoring Experiment-2 (GOME-2), effectively representing spatial, seasonal, and interannual vegetation variability. Our selection of CSIF was guided by its extensive spatial coverage, fine temporal resolution, and extended record length. Additionally, the data set maintains a high signal-to-noise ratio, providing robust and precise SIF estimates. By deriving from OCO-2 observations, CSIF retains the high-quality characteristics of the original satellite SIF data, offering a continuous and detailed depiction of vegetation photosynthetic activity. We utilize the full CSIF time series from 2000 to 2019 for all ecosystems without restricting analyses to specific seasons or growing-season windows. Long-term trends and seasonal variations were removed from the SIF data using seasonal-trend decomposition by Loess (STL) (Cleveland et al., 1990). We applied STL decomposition with a seasonal period of 92 (representing one year of data at 4-day intervals) to obtain residual time series for this analysis. The resulting detrended and deseasonalized anomaly time series represents short-term deviations from the local stable equilibrium state. Within this framework, perturbations are defined statistically as such short-term anomalies. This approach enables consistent estimation of CSD indicators across ecosystems with contrasting season lengths, including monsoon-driven tropical systems and high-latitude regions with short growing seasons. Because STL is applied independently at each pixel, the seasonal adjustment automatically adapts to local phenology, ensuring that resilience metrics are not biased by differences in growing-season timing or duration.

To focus our analysis specifically on vegetation resilience, we applied a natural vegetation mask derived from the MODIS land use-land cover product (MCD12C1) (Friedl & Sulla-Menashe, 2022). This data set utilizes the annual International Geosphere-Biosphere Programme (IGBP) land cover classification scheme to identify and isolate classes.

2.2. Climate and Soil Moisture Data

We employed the Köppen–Geiger climate classification (Köppen, 1936; Peel et al., 2007) to delineate major global climate zones. Climate variables, including precipitation, temperature, and vapor pressure deficit (VPD), were sourced from the Climatic Research Unit data set from the University of East Anglia (Harris et al., 2020), which provides monthly-scale data at a spatial resolution of 0.5° dating back to January 1901. Additionally, root zone soil moisture (RZSM) data were obtained from the Global Land Data Assimilation System (GLDAS), which integrates terrestrial and satellite-derived observations through land surface modeling and assimilation techniques to produce estimates of land surface states and fluxes. Specifically, we used daily GLDAS Version 2 data products at a spatial resolution of 0.25° (Li et al., 2018; Rodell et al., 2004). Our analysis utilized data spanning from 2000 to 2019.

2.3. Vegetation Resilience Estimation

To assess vegetation resilience, we utilized dynamical metrics rooted in CSD theory (Dakos et al., 2008; Scheffer et al., 2009). CSD suggests that as ecosystems approach a tipping point, their ability to recover from disturbances diminishes, resulting in slower system responses. This phenomenon can be detected through increased temporal autocorrelation and variance in the system's fluctuations (Boers & Rypdal, 2021; Smith et al., 2022).

We specifically evaluated the lag-one autocorrelation (AC1) and variance of residual SIF signals as key indicators. Their theoretical foundation lies in the linearization of the system near a stable equilibrium x^* , where small perturbations $\tilde{x} = x - x^*$ evolve according to the stochastic differential equation:

$$d\tilde{x} = \lambda\tilde{x}dt + \sigma dW \quad (1)$$

with λ representing the recovery rate, σ the standard deviation, and W the Wiener process. This defines an Ornstein–Uhlenbeck process, which, when discretized over time steps Δt , leads to closed-form expressions for the variance and AC1 autocorrelation, which are related to λ (Dijkstra, 2013; Gardiner, 1985):

$$\langle \tilde{x}^2 \rangle = \frac{\sigma^2}{2\lambda} \quad (2)$$

for the variance, and

$$\alpha(n) = e^{n\lambda\Delta t} \quad (3)$$

for the autocorrelation at lag n , thus $\alpha(1) = e^{\lambda\Delta t} = a = \text{AC1}$. Following the above formulations, the recovery rate was estimated using the variance-based approach with a defined time step Δt :

$$\lambda_{\text{var}} = -\frac{\sigma^2}{2\langle \tilde{x}^2 \rangle} \quad (4)$$

similarly for AC1 based:

$$\lambda_{\text{ac1}} = \log(a) \quad (5)$$

As the system becomes less stable, λ approaches zero. This decline in stability results in a sharp increase in the variance of fluctuations, $\langle \tilde{x}^2 \rangle$, which may trend toward infinity, and a corresponding rise in the lag-one autocorrelation, $\alpha(1)$, approaching a value of one. Such trends, marked by elevated variance and autocorrelation, act as early-warning signals of an impending critical transition. Accordingly, both indicators serve as valuable proxies for detecting shifts in system stability and resilience.

2.4. Trend Estimation of Vegetation Resilience

To assess shift in vegetation resilience over time, we applied the non-parametric Mann–Kendall trend (Kendall, 1948) test to time series (2000–2019) of (λ_{ac1}) and (λ_{var}) derived from residual of SIF data, specifically using a 3-year sliding window. This test is particularly suitable for this time series as it does not assume normality or linearity, and it is robust to missing values and outliers. For each resulting time series, the Mann–Kendall test was used to determine whether a statistically significant monotonic trend, either increasing or decreasing. The test computes Kendall's tau, a rank-based correlation coefficient, and the associated p-value. A p-value below 0.05 was considered statistically significant. We have shown the pixels which has $p < 0.05$.

To examine shifts in resilience trends over time, the analysis was conducted separately for two time periods: 2000–2009 and 2010–2019. The significance and direction of trends in each decade were evaluated individually. To detect shifts in resilience trends between the two decades, we computed the difference in Kendall's tau (τ), denoted as ΔTrend , for each pixel:

$$\Delta \text{Trend} = \tau_{2010-2019} - \tau_{2000-2009} \quad (6)$$

Both (λ_{ac1}) and (λ_{var}) typically range from negative values toward zero, with more negative λ values indicating faster recovery and thus higher resilience. Conversely, values closer to zero reflect slower recovery rates and reduced resilience, suggesting that the system is approaching a tipping point. Therefore, increasing trends in λ (i.e., λ becoming less negative) signal declining resilience, while decreasing trends (i.e., λ becoming more negative) imply increasing resilience. A positive ΔTrend indicates that the Kendall's tau value for the resilience indicator became more positive in the second decade (2010–2019) compared to the first (2000–2009). This can occur in two primary ways: (a) when an already positive trend, indicative of declining resilience becomes more positive, signaling an acceleration of resilience loss, and (b) when an initially negative trend, reflecting recovery, becomes less negative, reflecting deceleration of resilience gain; if the sign of the resilience trend reverses from negative to positive, it implies that a region has changes from increasing to decreasing recovery (i.e., reversal toward resilience loss). In both scenarios, a positive ΔTrend denotes a deterioration in resilience over time.

Conversely, a negative Δ Trend indicates that the τ value became more negative in the second decade, reflecting improved resilience. This arises under two primary scenarios: (a) if the trend was already negative, indicative of increasing resilience becomes more strongly negative, it suggests an acceleration of resilience gain; and (b) if the trend was initially positive, indicative of decreasing resilience but becomes less positive, it reflects a deceleration of resilience loss; if the sign of the resilience trend switches from positive to negative, it implies that a region has changes from decreasing to increasing recovery (i.e., reversal toward resilience gain). In both scenarios, a negative Δ Trend signifies improving resilience conditions over time. This approach allowed us to quantify and spatially map how the direction and strength of resilience trends have shifted, enabling detection of both nonlinear transitions (e.g., trend reversals) and gradual trend evolution (e.g., acceleration or stabilization) in vegetation resilience over time. For clarity, we provide representative examples illustrating each step of the resilience estimation workflow (Figures S1–S6 in Supporting Information S1). These examples show (a) the raw SIF time series, (b) STL-based decomposition and extraction of residual anomalies, (c) the resulting recovery-rate time series and its long-term trend (2000–2019), and (d–e) decade-specific trajectories (2000–2009 and 2010–2019) with corresponding trend lines and Kendall τ values. These examples represent the above mentioned characteristic trend-transition behaviors: (a) acceleration of resilience loss, (b) deceleration of resilience gain, (c) reversal toward resilience loss, (d) acceleration of resilience gain, (e) deceleration of resilience loss, (f) reversal toward resilience gain.

To investigate how climate and soil moisture changes relate to shifts in vegetation resilience, we computed the normalized percent trend per year for each variable across climate zone and LULC class combinations. For each group, we extracted spatially averaged 3 year rolling window from 2000 to 2019, applied min–max normalization. The Mann–Kendall test was used to assess monotonic trends, and Theil–Sen slope estimation was applied to quantify the trend magnitude. Slopes were then converted to percent change. This allowed direct comparison of trends across variables. By comparing the direction and magnitude of trends in λ against those in climate and soil moisture variables, we identified potential environmental drivers of resilience change.

3. Results

3.1. Global Spatial Patterns and Latitudinal Gradients in Recovery Rates

In the context of CSD theory, the recovery rate of a system, reflecting how quickly it returns to equilibrium following perturbations, can be inferred from statistical properties of time series data. Specifically, under the assumption of an Ornstein–Uhlenbeck process, both the AC1 and the variance of system fluctuations provide independent estimates of this recovery rate (λ). Throughout this study, we refer to these respective estimates as λ_{ac1} and λ_{var} .

Global maps of λ_{var} and λ_{ac1} recovery metrics reveal a pronounced latitudinal pattern of vegetation resilience (Figures 1a and 1b). The most negative values indicate the fastest return to equilibrium and, consequently, higher recovery rates. These values are predominantly clustered in the high-latitude boreal regions of North America and Russia. In contrast, λ values approach zero across the tropics and low latitudes in parts of South America, South Africa, Australia, and central Asia, indicating slower recovery. This hemispherically asymmetric pattern is captured in the zonal-mean transects (Figure 1 right panels). The resilience peaks around $\approx 60^\circ\text{N}$ and declines gradually toward the equator. Despite originating from distinct theoretical formulations, both λ_{var} and λ_{ac1} display highly coherent spatial distributions, reinforcing the internal consistency of the CSD framework when applied to SIF data. Consequently, the subsequent analyses in this study primarily utilize the variance-based recovery metric, λ_{var} .

Further clarity is achieved by disaggregating the zonal mean recovery rates according to LULC classes (Figure S7 in Supporting Information S1). Across all 10 natural vegetation types, resilience generally increases toward higher northern latitudes; however, the extent of this enhancement differs among LULC classes. This consistent pattern across both recovery indicators and LULC categories reveals a transparent, LULC-independent gradient: tropical ecosystems exhibit the slowest recovery rates. At the same time, high-latitude vegetation demonstrates a pronounced capacity for rapid post-disturbance recovery.

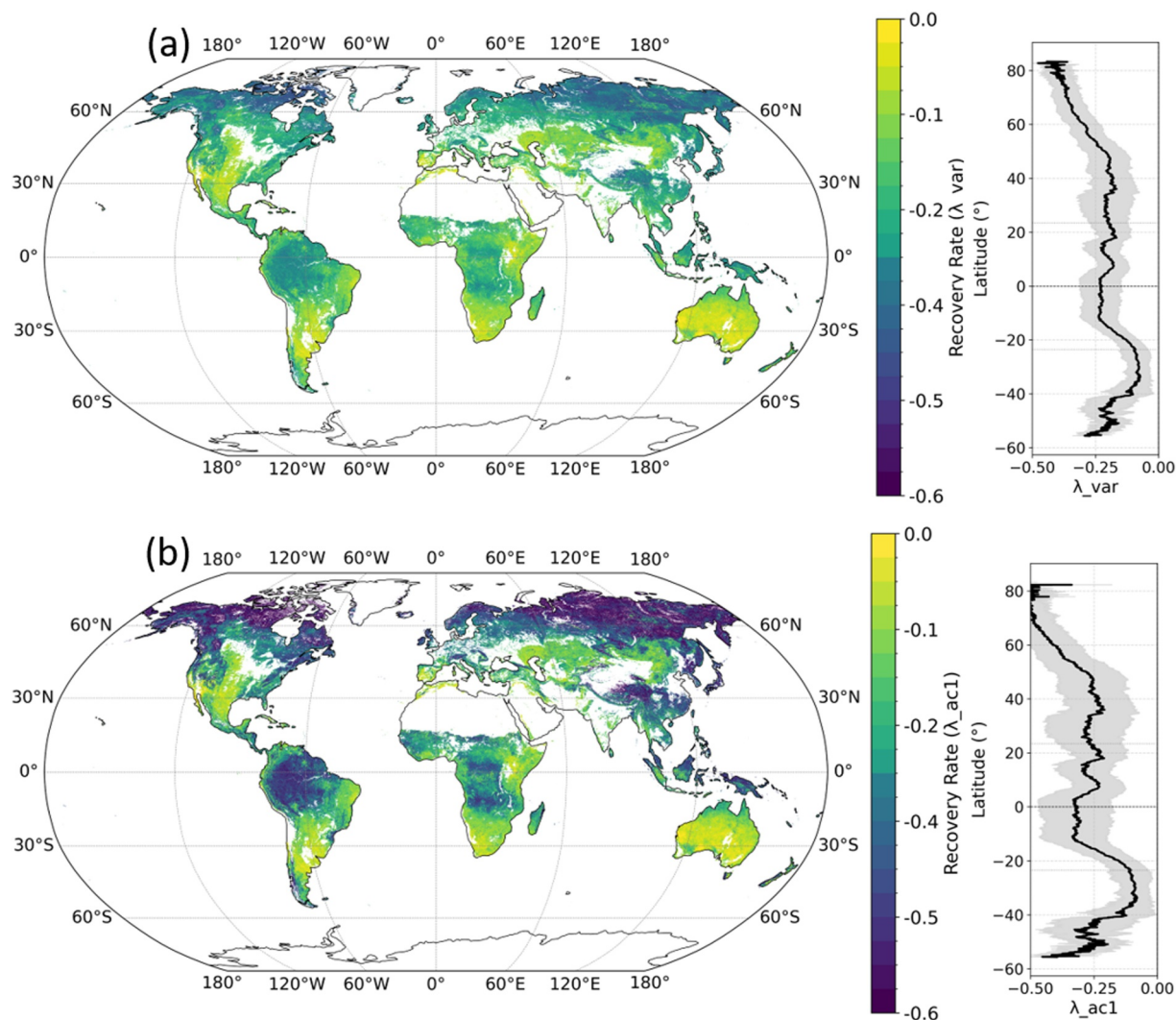


Figure 1. Spatial patterns and latitudinal gradients of vegetation recovery rates across global natural ecosystems. (a) Recovery rates estimated using variance-based indicators (λ_{var}) and (b) autocorrelation-based indicators (λ_{ac1}), derived from detrended and deseasonalized solar-induced chlorophyll fluorescence (SIF) time series. Maps illustrate pixel-level recovery potential, while the accompanying vertical plots depict zonal mean recovery rates as a function of latitude.

3.2. Global Shifts in Vegetation Resilience: Long-Term and Short-Term Trend

We first analyzed the long-term global trend in vegetation resilience using the SIF-derived recovery rate indicator (λ_{var}) over the full period from 2000 to 2019. The Mann–Kendall test was applied to the recovery rate time series at each pixel, revealing a spatially heterogeneous pattern of resilience change, with pronounced resilience loss in the Eurasian high latitudes and mixed signals in the global tropics (Figure 2a). Despite this heterogeneity, the global distribution of trends was found to be symmetric and balanced, with 52.6% of vegetated areas showing declining resilience (i.e., increasing (λ_{var})) and 47.4% showing improving resilience (i.e., decreasing (λ_{var})) (Figure 2b). This indicates the absence of a globally dominant trend direction but suggests divergent regional trajectories.

Further, to investigate how the resilience trend itself has evolved over time globally, we partitioned the study period into two decades: 2000–2009 and 2010–2019. For each pixel, the λ_{var} was calculated using a 3-year rolling window, and the Mann–Kendall τ statistic was estimated separately within each decade. Only pixels exhibiting statistically significant trends in both decades were retained. We then computed the difference between the two τ values, referred to as $\Delta\text{Trend} = \tau_{2010-2019} - \tau_{2000-2009}$, to quantify changes in the direction of resilience trends over time. The spatial patterns of significant positive and negative trends for each decade are shown in Figure S8

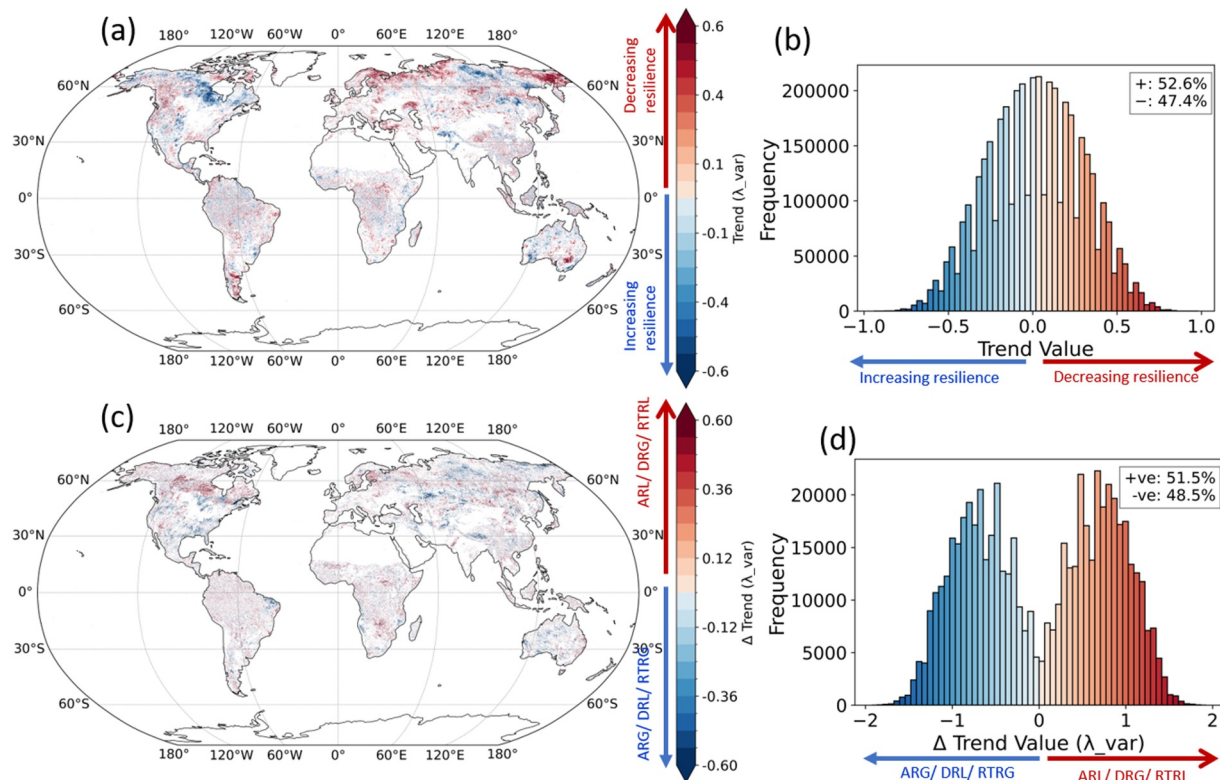


Figure 2. Spatial distribution of vegetation resilience trends and their temporal shifts based on SIF-derived variance estimates. (a) Global spatial pattern of statistically significant positive and negative long-term trends (2000–2019) for variance-based recovery rates λ_{var} , where positive Kendall's τ values indicate increasing λ_{var} (i.e., slower recovery and thus declining resilience), while negative values indicate decreasing λ_{var} (i.e., faster recovery and improving resilience). (b) Histogram of long-term resilience trends. (c) Spatial distribution of trend trajectory changes (Δ Trend), calculated as the difference in Kendall's τ between 2010–2019 and 2000–2009. (d) Histogram of Δ Trend values. Trends were estimated using the Mann–Kendall test. Only statistically significant trends ($p < 0.05$) are shown. Note: Positive Δ Trend values indicate either ARL: acceleration of resilience loss, or DRG: deceleration of resilience gain, or RTRL: reversal toward resilience loss. Negative Δ Trend values indicate either ARG: acceleration of resilience gain, or DRL: deceleration of resilience loss, or RTRG: reversal toward resilience gain.

in Supporting Information S1, highlighting areas where resilience has declined (positive trends) or improved (negative trends). The analysis of changes in resilience trend trajectories between the two decades reveals spatially heterogeneous and complex patterns of vegetation response (Figure 2c in Supporting Information S1). A positive Δ Trend indicates that the Kendall's τ value for the resilience indicator became more positive in the second decade (2010–2019) compared to the first (2000–2009). This can occur in two primary ways: (a) when an already positive trend, indicative of declining resilience becomes more positive, signaling an acceleration of resilience loss, and (b) when an initially negative trend, reflecting recovery, becomes less negative, reflecting deceleration of resilience gain; if the sign of the resilience trend reverses from negative to positive, it implies that a region has changes from increasing to decreasing recovery (i.e., reversal toward resilience loss). In both scenarios, a positive Δ Trend denotes a deterioration in resilience over time.

Conversely, a negative Δ Trend indicates that the τ value became more negative in the second decade, reflecting improved resilience. This arises under two primary scenarios: (a) if the trend was already negative, indicative of increasing resilience becomes more strongly negative, it suggests an acceleration of resilience gain; and (b) if the trend was initially positive, indicative of decreasing resilience but becomes less positive, it reflects a deceleration of resilience loss; if the sign of the resilience trend switches from positive to negative, it implies that a region has changes from decreasing to increasing recovery (i.e., reversal toward resilience gain). In both scenarios, a negative Δ Trend signifies improving resilience conditions over time. The global spatial pattern highlights contrasting trajectories in resilience trend dynamics, with regions showing deterioration in resilience (positive Δ Trend; red areas) concentrated in parts of boreal North America, Asia, Southern Africa, and Australia, while regions exhibiting trend reversal toward improving resilience (negative Δ Trend; blue areas) are prominent in parts of South America, Western Australia, and Russia.

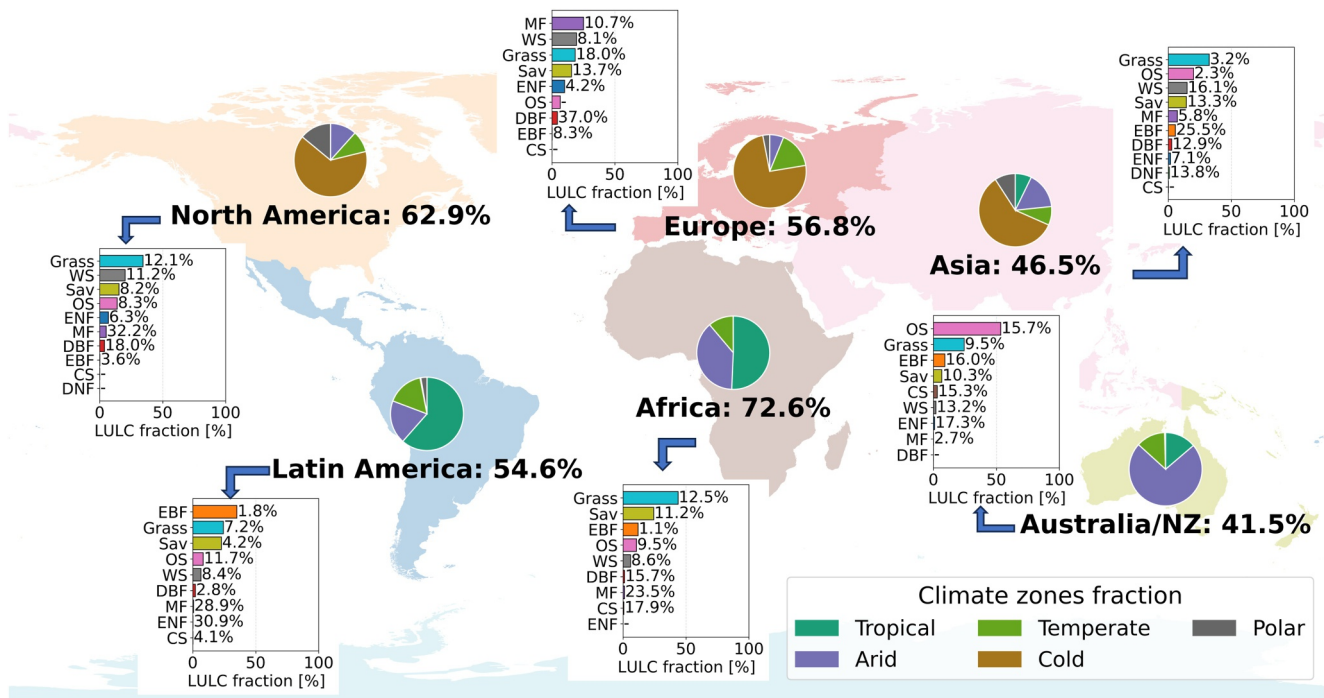


Figure 3. Spatial summary of positive Trend (indicative of resilience loss) in variance-based SIF resilience (λ_{var}) during 2000–2019 across six global regions. For each region, the centroid is accompanied by a climate-zone pie chart summarizing the fractional contribution of dominant Koppen-Geiger climate classes, while adjacent bar charts depict the overall land-cover composition; numbers at the end of each bar indicate the proportional contribution of individual land-cover classes to regional resilience loss. Labels beneath each pie chart report the total percentage of grid cells in that region with a positive resilience trend.

The distribution of Δ Trend values (Figure 2d) is bimodal and centered around zero, indicating two dominant and opposing directions of trend evolution. While 51.5% of vegetated pixels exhibit positive Δ Trend, signaling either an accelerated resilience decline, deceleration in recovery, or a shift from recovery to deterioration, 48.5% show negative Δ Trend, consistent with either an acceleration in recovery, deceleration of resilience loss, or a transition toward recovery. This near-symmetric yet bimodal distribution indicates that while the global average trend shift remains balanced, ecosystems are increasingly diverging in their resilience trajectories. These findings underscore the nonlinear, region-specific nature of resilience dynamics under recent climatic and anthropogenic pressures.

While the global patterns of both the long-term trend and Δ Trend appear relatively balanced, we further examined how these proportions vary across different regions to uncover spatial heterogeneity in resilience trends and their dynamics. Building upon the spatial and temporal trends in resilience change, we conducted a regional analysis by quantifying the proportion of pixels exhibiting a positive trend (decreasing resilience) in variance-based recovery rates across six major global regions (Figure 3). For each region, the centroid is accompanied by a climate-zone pie chart summarizing the fractional contribution of dominant Koppen-Geiger climate classes, while adjacent bar charts depict the overall land-cover composition. The numbers next to each bar indicate the proportional contribution of land-cover classes to regional resilience loss. The extent of recovery loss in the recent decade varies substantially across regions, with Africa and North America exhibiting the highest proportions of affected pixels (72.6% and 62.9%, respectively), while Asia and Australia/New Zealand show lower values (46.5% and 41.5%, respectively). Europe and Latin America lie in between, with 56.8% and 54.6% of pixels indicating resilience loss. The bar charts indicate that the resilience declines are not uniformly distributed but are concentrated in specific land-cover types within each region. In Africa, grasslands are of particular concern, not only because they dominate the landscape, but also because a significant proportion of their area is experiencing resilience loss. Shrublands and mixed forest (MF), though covering a smaller proportion of the area, also account for a substantial share of pixels experiencing decline, highlighting the vulnerability of multiple ecosystem types. In North America, deciduous broadleaf forests (DBF) and MF, despite their limited spatial extent, contribute disproportionately to overall resilience loss, highlighting the risk faced by these critical forest systems in the

recent decade. Here, too, the dominant grasslands are undergoing significant resilience loss. Europe and Asia reveal a similar pattern, where significant declines are concentrated in DBF and evergreen broadleaf forests (EBF), respectively, both of which occupy only a modest fraction of the landscape yet play vital ecological roles. In Australia and New Zealand, it is a different scenario: open shrublands, which span a vast portion of the region, emerge as the primary contributor of resilience decline. Notably, across several continents, the resilience loss is not driven by a single dominant LULC class but rather reflects a fragmented pattern, with contributions from multiple land-cover types, including those with relatively small spatial extents. This disproportionate impact of both major and minor land cover classes signals a dual threat: systemic risks to broad ecosystem function and stability, and the potential loss of unique, sensitive habitats that underpin regional biodiversity and ecological resilience. The middle rings contextualize these declines against the background land-cover distributions, highlighting the disproportionate vulnerability of certain vegetation types. The pie charts relate these patterns to climate, showing that Africa, with the highest proportion of resilience loss, is largely dominated by tropical climates.

Additionally, we present an analogous regional summary based on Δ Trend (Figure S9 in Supporting Information S1), where the bar and pie charts follow the same conventions as the long-term trend figure (Figure 3), representing the overall land-cover composition and dominant Köppen climate zones, respectively. However, the numbers next to each bar here depicts the proportion of each land-cover class experiencing an acceleration of resilience loss or deceleration in recovery (or reversal, i.e., shift from resilience gain to resilience loss) between the two decades. Here too, Africa (64.0%) and North America (60.8%) show the largest proportions of area undergoing either an acceleration of resilience loss or deceleration in recovery or a reversal toward loss. Overall, this perspective highlights regions and their associated LULC types where resilience trajectories are worsening more rapidly in recent years, revealing emerging vulnerabilities that may not be evident from long-term trends alone. For example, in Africa and Europe, the proportion of grasslands showing decreasing resilience in the long-term trend is substantial, yet an even greater proportion is experiencing acceleration of resilience loss, or deceleration in recovery, or a reversal toward loss indicating that deterioration is intensifying (Compare Figure 3 and Figure S9 in Supporting Information S1). A similar pattern is observed for DBF in America, shrublands in Australia/NZ, and EBF in Asia. When the share of area undergoing acceleration of resilience loss exceeds that of overall decline, it signals that these ecosystems are entering a more critical stage of vulnerability, either losing resilience at a faster rate or reversing from recovery to decline in the recent decade, highlighting the urgency for timely management and intervention. By integrating both the proportion of vulnerable area and the underlying landscape composition, this analysis highlights the complex and regionally varied nature of the rate of resilience decline, underscoring the urgent need for targeted conservation strategies that address the risks facing both dominant ecosystems and more vulnerable, less extensive vegetation types across the globe. The pie charts relate these patterns to climate, showing that Africa, with the highest proportion of acceleration of resilience decline or deceleration in recovery or a reversal, is largely dominated by tropical climates, whereas Asia, exhibiting the lowest proportion of decline, falls predominantly within cold climate zones. Collectively, these findings underscore that changes in vegetation resilience are strongly influenced by regional LULC characteristics and climatic conditions, reflecting complex interactions among ecosystem structure, climate stressors, and anthropogenic impacts. This is consistent with the mechanisms proposed in prior studies (Han et al., 2025; Hirota et al., 2011).

3.3. Interplay of LULC, and Climatic Drivers in Vegetation Resilience Shifts

To further elucidate how shifts in resilience trend vary across vegetation types and climatic contexts, we examined land cover-specific changes in the variance-based recovery rate trend (Δ Trend) within major global climate zones (Figure 4). Figure 4a presents the distribution of Δ Trend values for each LULC class across five primary climate zones: tropical, arid, temperate, cold, and polar. The zero reference line demarcates the threshold between acceleration of resilience decline or recovery loss (positive Δ Trend) and improvement (negative Δ Trend). In tropical climates, both the mean and median Δ Trend values for nearly all LULC classes lie above this reference line, indicating that the majority of pixels within these vegetation types are experiencing an acceleration of decline in resilience or deceleration of resilience gain or a reversal toward loss. This consistent upward shift signals widespread stress across tropical ecosystems, with shrublands being a notable exception, showing comparatively lower levels of resilience loss. Figure 4b provides a complementary view by summarizing the relative proportion of pixels within each climate zone that exhibit significant acceleration of decline in resilience or deceleration of

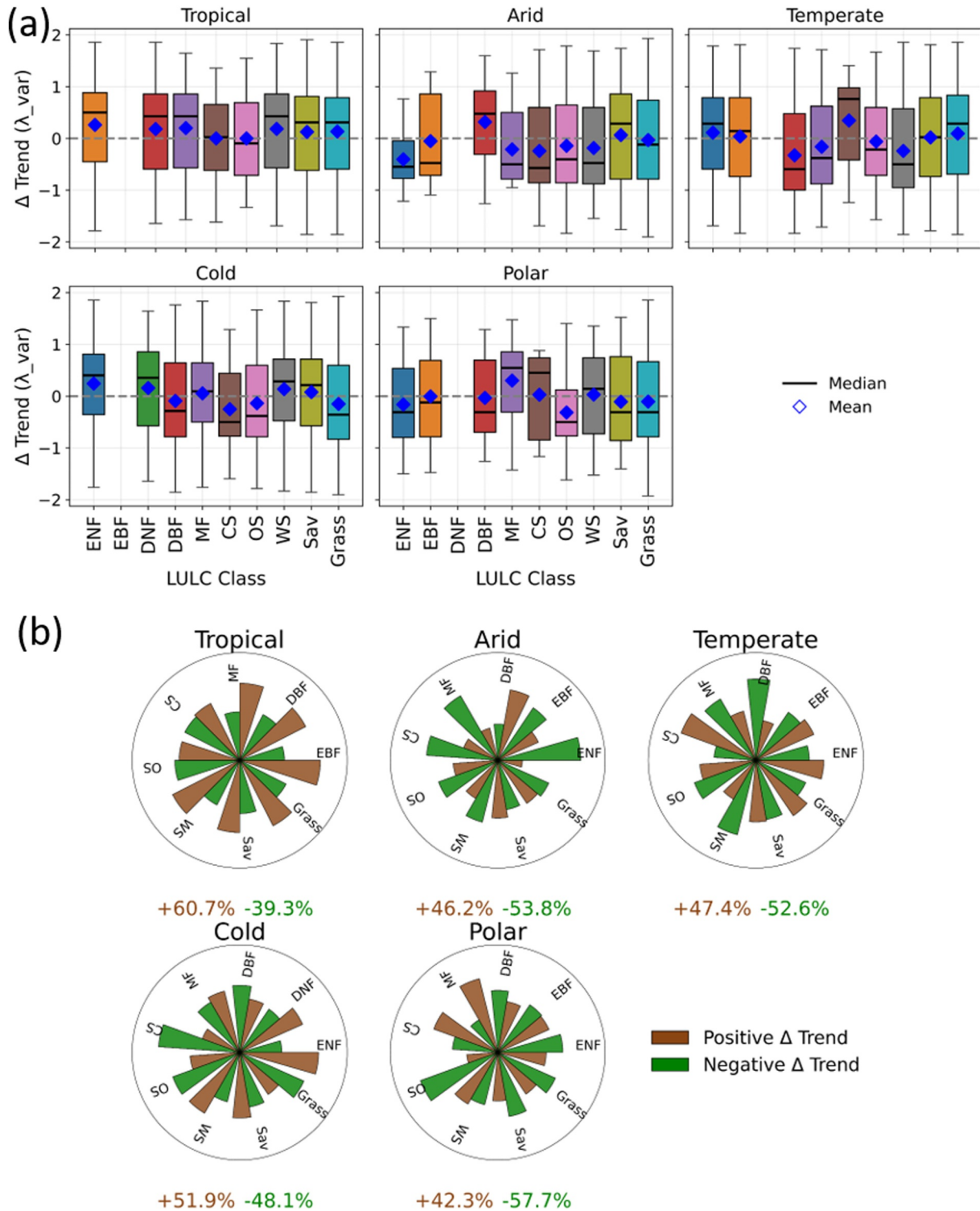


Figure 4. Land cover-specific shifts in vegetation resilience trends across major global climate zones. (a) Bar chart showing the distribution of Δ Trend in variance-based recovery rates (λ_{var}) across major climate zones, stratified by land use and land cover (LULC) types. A gray reference line at zero indicates the balance between positive and negative Δ trends. Panel (b) Stacked bars represent the proportion of area within each climate zone exhibiting significant positive (brown) and negative (green) Δ Trends, disaggregated by LULC class. Total area percentages per climate zone are indicated below each subplot. Note: Positive Δ Trend values indicate either ARL: acceleration of resilience loss, or DRG: deceleration of resilience gain, or RTRL: reversal toward resilience loss. Negative Δ Trend values indicate either ARG: acceleration of resilience gain, or DRL: deceleration of resilience loss, or RTRG: reversal toward resilience gain.

resilience gain or a reversal toward resilience loss (brown) versus stabilization or gain (green), stratified by LULC class. The tropical zone shows the highest proportion of affected area, with approximately 60.7% of pixels undergoing resilience loss in the recent decade. In contrast, polar regions exhibit lower fractions of decline (approximately 42.3%). Consistent with the Δ Trend in Figure 4a, all tropical land cover types, except shrubland, show high proportions of an acceleration of decline in resilience or deceleration of resilience gain or a reversal toward resilience loss. Notably, several vegetation types, including evergreen needleleaf forests, deciduous broadleaf forests, savannas, and grasslands, display divergent resilience trajectories across different climate zones. These contrasting patterns underscore the climate-dependent sensitivity of specific LULC types to environmental stressors, highlighting the need to account for both vegetation structure and climatic context when assessing ecosystem resilience.

This overall pattern is supported by detailed LULC-specific distributions of Δ Trend within the tropical climate zone (Figure S10 in Supporting Information S1). Histograms for each major vegetation class reveal the percentage of area exhibiting positive (acceleration of decline in resilience or deceleration of resilience gain or a reversal toward resilience loss) and negative (deceleration of declining resilience or acceleration of resilience gain or reversal toward resilience gain) Δ Trend. Consistent with the main figure (Figure 4), broadleaf evergreen forests, savannas, and grasslands show a majority of pixels with acceleration of decline in resilience or deceleration in recovery or a reversal toward resilience loss, whereas shrublands display a more balanced or slightly improving resilience pattern. These findings emphasize the complex interplay between vegetation composition and climate in shaping regional ecosystem resilience dynamics. The pronounced acceleration of resilience decline across most tropical vegetation types signals heightened vulnerability of these ecosystems to ongoing climatic stresses, whereas the more mixed trends observed in arid, temperate, cold, and polar zones suggest diverse adaptive capacities and responses among LULC.

Given the pronounced loss of vegetation resilience observed in the tropical regions, we further investigated the underlying dynamics by analyzing normalized time series of variance-based recovery rates (λ_{var}) alongside key climatic drivers, that is, precipitation (Prec), temperature (Temp), vapor pressure deficit (VPD), and soil moisture (SM), for each LULC class within this region (Figure 5a). The percentages indicated in each subplot denote the fractional area of the tropical region occupied by the respective LULC type. Prominent vegetation classes such as evergreen broadleaf forest (EBF), woody savanna (WS), savanna (Sav), and grassland show significant positive trends in λ_{var} (indicated by Theil–Sen slope), coinciding with increasing temperature and VPD trends (also positive Theil–Sen slopes), coupled with declines in precipitation and soil moisture (negative Theil–Sen slopes). To rigorously assess the significance of these trends, we applied the Kendall's tau test, which evaluates the consistency and statistical robustness of the monotonic changes over time. Only trends passing this significance threshold were considered, ensuring our interpretations reflect meaningful temporal shifts rather than random fluctuations.

The complementary Theil–Sen slope analysis (Figure 5b), presented as percentage change per year, supports these findings by quantifying the magnitude of change across all variables. Together, these results reveal that key tropical LULC types are experiencing a reduction in resilience aligned with warming and drying climate conditions. This combined statistical evidence underscores the heightened vulnerability of tropical ecosystems to ongoing climatic stressors and highlights the urgent need to monitor and manage these critical LULC under accelerating environmental change.

4. Discussion

Our analysis reveals significant spatial and temporal heterogeneity in vegetation functional resilience across global natural ecosystems, as captured by SIF data. Using dynamical system theory and CSD indicators, we provide robust estimates of vegetation recovery rates, their trends, and trend trajectories over two recent decades (2000–2009 and 2010–2019). The latitudinal gradients and LULC-specific patterns observed in our study emphasize the complex interplay between climate, vegetation type, and resilience dynamics under changing environmental conditions.

The pronounced latitudinal pattern in recovery rates (Figure 1), with higher resilience in boreal regions and lower resilience in tropical zones, aligns well with prior studies reporting LULC and climate-dependent recovery dynamics (Seddon et al., 2016). The faster recovery rates of boreal forests may reflect adaptations to extreme seasonal climates and disturbance regimes, which have shaped resilient ecosystem structures (Johnstone

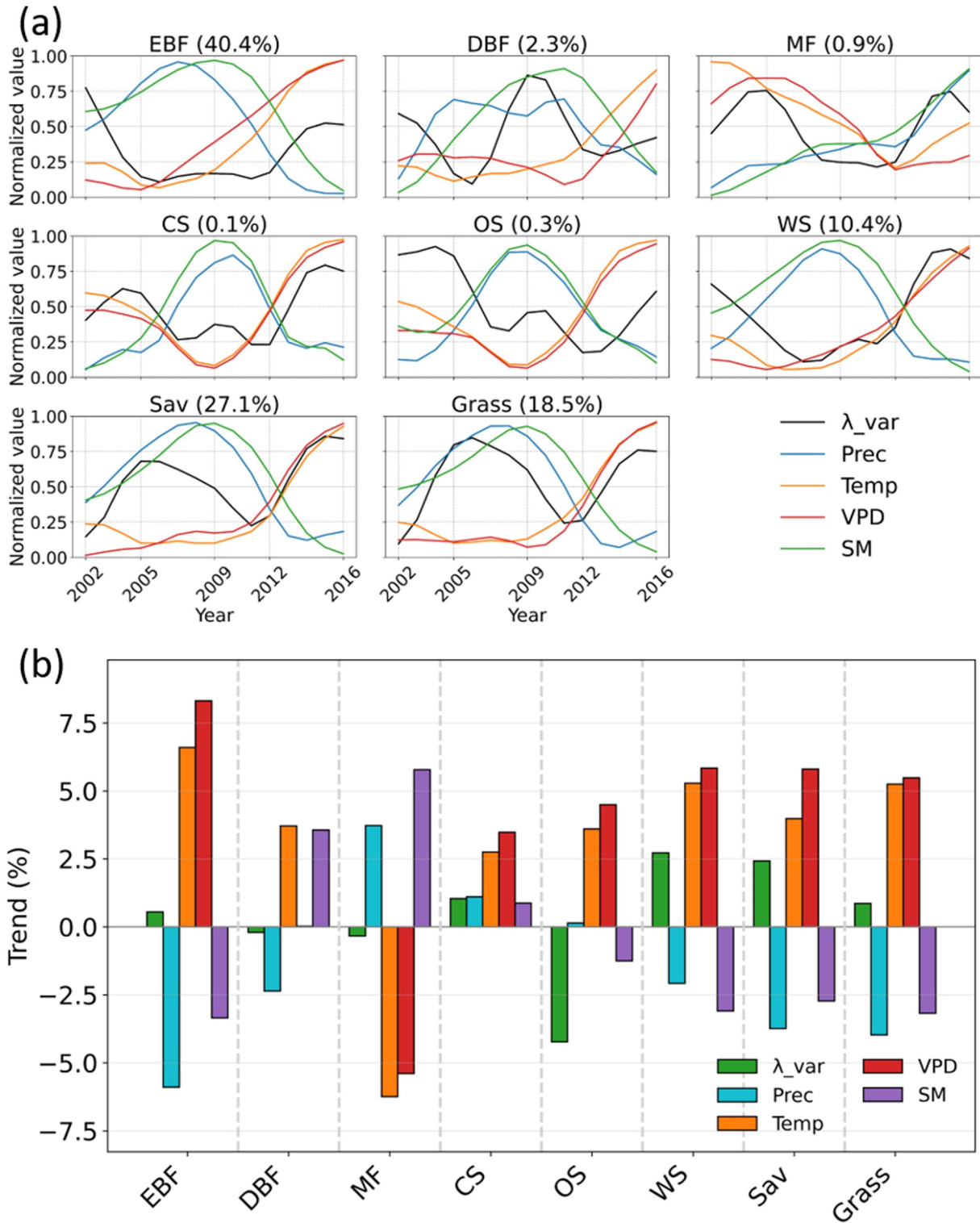


Figure 5. Temporal dynamics and trends of vegetation recovery and climate drivers in tropical climate zones. (a) Time series of normalized variance-based recovery rates (λ_{var}), precipitation (Prec), temperature (Temp), vapor pressure deficit (VPD), and soil moisture (SM), averaged across LULC types within the tropical climate zone using a 3-year rolling window. Percent values in the upper right corner of each subplot indicate the proportion of the tropical zone occupied by each LULC type. (b) Corresponding percentage trends (estimated by Sen's slope) for each variable across LULC categories, highlighting the direction and magnitude of change over time.

et al., 2016). These ecosystems tend to possess species with life-history traits geared toward rapid recovery and regeneration following disturbances (Engelmark, 1999). Conversely, tropical ecosystems exhibit slower recovery rates, consistent with their typically high biodiversity but also vulnerability to prolonged drought and anthropogenic pressures (Brando et al., 2014; Phillips et al., 2009). The slow recovery may also be linked to the complex species interactions and nutrient cycling dynamics in tropical forests, which can be disrupted by climatic extremes (Bonan, 2008). Additionally, these forests are often closer to physiological thresholds for heat and water stress, making them more susceptible to compounded climatic impacts (Corlett, 2016; Doughty et al., 2023). Stratification by LULC further refines this pattern, revealing LULC-specific resilience gradients within climate zones (Figure 4). Our findings that tropical broadleaf forests, savannas, and grasslands show marked acceleration of resilience declines or recovery loss underscore the sensitivity of these ecosystems to recent climate variability and land use change (Lewis et al., 2011). These results echo previous remote sensing and field-based observations documenting forest degradation and altered disturbance regimes in tropical regions (Aragão et al., 2018).

By analyzing both the long-term recovery trends and the changes in trend trajectories between decades, we reveal spatially heterogeneous resilience dynamics at both global and regional scales (Figure 2). The near balance between areas of resilience loss and gain highlights the non-uniform responses of ecosystems to environmental change. For example, regions such as boreal North America and parts of Asia show both resilience declines and gains (Figures 2a and 2b), reflecting local climatic variability and disturbance legacies (Beck et al., 2011; Zhang et al., 2024). These mixed patterns suggest that ecosystem responses are shaped by a complex interplay of natural disturbance regimes, climate variability, and possibly land management practices. While long-term trends provide insights into the net direction of resilience change, the Δ Trend analysis captures underlying shifts in trajectory, such as accelerations, decelerations, or reversals, that may signal emerging vulnerabilities. This is particularly important in regions where ecosystems appear stable over the long term but are showing early signs of slowdown or trend reversal toward resilience loss in recent decades (compare Figures 2a and 2c, and also compare Figure 2 and Figure S8 in Supporting Information S1). These dynamics, visible only through Δ Trend, underscore the need to analyze both static trend assessments and detect evolving risks. The regional analysis (Figure 3 and Figure S9 in Supporting Information S1) further elucidates that the percentage of area undergoing resilience loss and accelerated resilience decline is not uniformly distributed and is strongly influenced by the underlying land-cover composition and dominant climate regimes. In Africa, both widespread grasslands and less extensive shrublands contribute substantially to resilience loss, while in North America, the resilience decline largely takes place in deciduous broadleaf and mixed forests, despite their smaller spatial coverage. Europe and Asia show a similar pattern, with notable losses concentrated in deciduous and evergreen broadleaf forests, even though these types occupy a limited portion of the landscape. This points to the importance of vegetation structure and composition in mediating regional ecosystem resilience (Bai et al., 2004; García-Palacios et al., 2018). This uneven distribution of recovery loss and acceleration of resilience loss calls for targeted, biome-specific conservation strategies to protect both widespread and less extent ecosystems that are showing early signs of rapid decline.

Our detailed analysis of tropical climate zone dynamics reveals consistent associations between declining vegetation resilience and warming, increased vapor pressure deficit (VPD), and reduced precipitation and soil moisture (Figure 5). This pattern corroborates the growing body of literature highlighting drought and heat stress as key drivers of tropical forest vulnerability (Brando et al., 2025; Phillips et al., 2009). The strong concordance between increasing temperature and VPD trends with positive λ_{var} slopes suggests that intensifying climatic stress is eroding the capacity of tropical ecosystems to recover from disturbances. The use of robust trend detection methods, including Mann–Kendall significance testing and Theil–Sen slope estimation, strengthens the reliability of these findings. The acceleration of resilience decline in major tropical vegetation types such as evergreen broadleaf forests and savannas has profound implications for global carbon cycling, biodiversity conservation, and climate feedback (Bazzaz, 1998). Moreover, reduced resilience threatens biodiversity conservation by compromising habitat stability, species composition, and ecosystem services fundamental to both local livelihoods and global ecological balance (Gatti et al., 2021). The synergistic effects of warming, drying, and increased atmospheric demand exacerbate physiological stress on tropical vegetation, increasing the likelihood of regime shifts, forest dieback, and loss of ecosystem function and associated ecosystem services (Cusack et al., 2016). These outcomes underscore the urgent need for monitoring and adaptive management strategies aimed at mitigating climate impacts and preserving the resilience of tropical ecosystems under accelerating global change. Our estimates are based on functional resilience derived from detrended and deseasonalized photosynthetic activity.

Increases in variance or autocorrelation may therefore sometimes reflect natural internal variability or ongoing successional processes, rather than a true deterioration of ecosystem resilience. This is particularly relevant in ecosystems where structural recovery and species turnover occur over multi-decadal timescales. Therefore, our results should be interpreted as changes in the short-term functional resilience of vegetation in terms of photosynthesis, not as comprehensive indicators of broader ecosystem resilience that includes compositional, structural, and biodiversity-related dimensions (Guo et al., 2021; Kim et al., 2024; Woodgate et al., 2025). Further, while SIF provides a valuable physiological indicator of photosynthetic activity, it is important to acknowledge several caveats. SIF is not a direct measurement of carbon assimilation or Rubisco-limited photosynthesis; rather, it reflects chlorophyll fluorescence emitted during the light reactions and is modulated by both photochemical and non-photochemical pathways. As previous studies have shown (Jones et al., 2023; Marrs et al., 2020), relationships between SIF and carbon assimilation can weaken under conditions of high heat stress, strong non-photochemical quenching, or stomatal closure, when fluorescence yield may increase even as carbon uptake declines. In addition, because satellite-retrieved SIF is derived from canopy reflectance, it retains some spectral and structural sensitivities, including potential influences of biomass, viewing geometry, and canopy architecture. These caveats highlight that, although SIF can offer earlier and more physiologically relevant stress detection than greenness-based indices, it does not represent a direct or universal measure of carbon assimilation, and should be interpreted as an indicator of photosynthetic function rather than a precise measure of ecosystem carbon uptake. Despite these limitations, SIF remains well suited for resilience diagnostics because it captures rapid physiological regulation of photosynthetic function in response to environmental perturbations. By analyzing recovery dynamics of detrended SIF anomalies, we focus on the temporal stability of photosynthetic activity rather than its absolute magnitude.

Our study highlights recent global shifts in vegetation functional resilience and their trends as revealed by SIF. By integrating CSD theory with robust statistical trend analysis, our study offers a framework for early detection of ecosystem destabilization under climate and land use composition. The observed LULC and climate zone-specific patterns underscore the necessity for targeted conservation and adaptive management strategies that consider ecosystem-specific vulnerabilities and climate projections. Beyond testing theoretical expectations of CSD, the global resilience patterns revealed in this study provide a practical foundation for advancing ecosystem monitoring and understanding. First, the spatially explicit declines and gains in functional resilience offer a strategic basis for targeted regional-scale investigations aimed at identifying the ecological and climatic mechanisms underlying emerging vulnerabilities. Second, because changes in functional resilience often precede observable shifts in ecosystem state, our framework establishes an operational early-warning context for detecting regions at heightened risk under increasing climate pressure. These insights can inform the prioritization of field campaigns, long-term monitoring efforts, and the allocation of conservation or management resources. By outlining where resilience is eroding and how these trajectories are evolving, the analysis provides a platform for future observational, experimental, and modeling work, positioning functional resilience as a meaningful lens through which to evaluate ecosystem stability in a changing climate. Moreover, expanding analyses to include anthropogenic drivers such as land use intensification, fire regimes, and invasive species will enhance understanding of resilience loss mechanisms (Oliver et al., 2015). Coupling these resilience indicators with predictive ecosystem models may improve forecasting of tipping points and guide proactive interventions.

5. Conclusion

We leveraged SIF, an indicator of photosynthetic activity, to assess global vegetation functional resilience from 2000 to 2019. By applying indicators of CSD, we calculated recovery rates from variance and autocorrelation in SIF time series. Our analysis revealed strong latitudinal contrasts, with boreal ecosystems recovering more rapidly while tropical and low-latitude ecosystems remained persistently vulnerable. Long-term trends highlighted pronounced resilience declines in the Eurasian high latitudes, whereas short-term trajectories exposed diverging pathways, with some ecosystems showing recovery and others accelerating toward loss. In particular, tropical ecosystems experienced widespread and worsening declines linked to rising heat, vapor pressure deficits, and soil moisture stress. Together, these findings establish a framework for early detection of ecosystem destabilization, providing critical guidance for global conservation, management, and climate adaptation.

Conflict of Interest

The authors declare no conflicts of interest relevant to this study.

Availability Statement

All the data utilized in this study were sourced from publicly available data sets. CSIF data set can be accessed at Zhang et al. (2018). MODIS LULC can be downloaded from Friedl and Sulla-Menashe (2022). Soil moisture data is available at Li et al. (2018). Precipitation, temperature, and VPD data can be accessed at Harris et al. (2020). The code for this research is available in this link: <https://doi.org/10.5281/zenodo.17924041> (Behera & Dutta, 2025).

Acknowledgments

S. Behera acknowledges the research fellowship support from the Prime Minister's Research Fellowship (PMRF) by the Ministry of Education, Government of India, at the Indian Institute of Science (IISc). D. Dutta acknowledges Indian Institute of Science Seed-grant and Institute of eminence Grant IE/REDA-25-0012 and the DST-Science and Engineering Research Board Grant SRG/2021/000328 for supporting this research.

References

- Allen, C. D., Macalady, A. K., Chenchouni, H., Bachelet, D., McDowell, N., Vennetier, M., et al. (2010). A global overview of drought and heat-induced tree mortality reveals emerging climate change risks for forests. *Forest Ecology and Management*, 259(4), 660–684. <https://doi.org/10.1016/j.foreco.2009.09.001>
- Aragão, L. E., Anderson, L. O., Fonseca, M. G., Rosan, T. M., Vedovato, L. B., Wagner, F. H., et al. (2018). 21st Century drought-related fires counteract the decline of Amazon deforestation carbon emissions. *Nature Communications*, 9(1), 536. <https://doi.org/10.1038/s41467-017-02771-y>
- Bai, Y., Han, X., Wu, J., Chen, Z., & Li, L. (2004). Ecosystem stability and compensatory effects in the Inner Mongolia grassland. *Nature*, 431(7005), 181–184. <https://doi.org/10.1038/nature02850>
- Bazzaz, F. (1998). Tropical forests in a future climate: Changes in biological diversity and impact on the global carbon cycle. *Climatic Change*, 39(2), 317–336. <https://doi.org/10.1023/a:1005359605003>
- Beck, P. S., Juday, G. P., Alix, C., Barber, V. A., Winslow, S. E., Sousa, E. E., et al. (2011). Changes in forest productivity across Alaska consistent with biome shift. *Ecology Letters*, 14(4), 373–379. <https://doi.org/10.1111/j.1461-0248.2011.01598.x>
- Behera, S., & Dutta, D. (2024). Tracking gross primary productivity using satellite solar induced fluorescence: Insights across agricultural ecosystems of India. *Journal of Geophysical Research: Biogeosciences*, 129(5), e2023JG007586. <https://doi.org/10.1029/2023jg007586>
- Behera, S., & Dutta, D. (2025). Code: Photosynthetic recovery dynamics reveal declining vegetation functional resilience in tropical ecosystems [Dataset]. *Zenodo*. <https://doi.org/10.5281/zenodo.17924041>
- Behera, S., Elakkiyaa, T. L., Sarkar, A., & Dutta, D. (2025). Solar-induced chlorophyll fluorescence yield holds the potential for drought early warning. *Geophysical Research Letters*, 52(4), e2024GL113419. <https://doi.org/10.1029/2024gl113419>
- Boers, N., Ghil, M., & Stocker, T. F. (2022). Theoretical and paleoclimatic evidence for abrupt transitions in the Earth system. *Environmental Research Letters*, 17(9), 093006. <https://doi.org/10.1088/1748-9326/ac8944>
- Boers, N., & Rypdal, M. (2021). Critical slowing down suggests that the western Greenland Ice Sheet is close to a tipping point. *Proceedings of the National Academy of Sciences*, 118(21), e2024192118. <https://doi.org/10.1073/pnas.2024192118>
- Bonan, G. B. (2008). Forests and climate change: Forcings, feedbacks, and the climate benefits of forests. *Science*, 320(5882), 1444–1449. <https://doi.org/10.1126/science.1155121>
- Brando, P. M., Balch, J. K., Nepstad, D. C., Morton, D. C., Putz, F. E., Coe, M. T., et al. (2014). Abrupt increases in Amazonian tree mortality due to drought–fire interactions. *Proceedings of the National Academy of Sciences*, 111(17), 6347–6352. <https://doi.org/10.1073/pnas.1305499111>
- Brando, P. M., Barlow, J., Macedo, M. N., Silvério, D. V., Ferreira, J. N., Maracahipes, L., et al. (2025). Tipping points of Amazonian forests: Beyond myths and toward solutions. *Annual Review of Environment and Resources*, 50(1), 97–131. <https://doi.org/10.1146/annurev-environ-111522-112804>
- Carpenter, S. R., Cole, J. J., Pace, M. L., Batt, R., Brock, W. A., Cline, T., et al. (2011). Early warnings of regime shifts: A whole-ecosystem experiment. *Science*, 332(6033), 1079–1082. <https://doi.org/10.1126/science.1203672>
- Chen, Z., Fan, P., Hou, X., Ji, F., Li, L., Qian, Z., et al. (2024). Analysis of global vegetation resilience under different future climate scenarios. *Climate Dynamics*, 62(8), 7967–7980. <https://doi.org/10.1007/s00382-024-07317-9>
- Cleveland, R. B., Cleveland, W. S., McRae, J. E., & Terpenning, I. (1990). STL: A seasonal-trend decomposition. *Journal of Official Statistics*, 6(1), 3–73.
- Corlett, R. T. (2016). The impacts of droughts in tropical forests. *Trends in Plant Science*, 21(7), 584–593. <https://doi.org/10.1016/j.tplants.2016.02.003>
- Cusack, D. F., Karpman, J., Ashdown, D., Cao, Q., Ciochina, M., Halterman, S., et al. (2016). Global change effects on humid tropical forests: Evidence for biogeochemical and biodiversity shifts at an ecosystem scale. *Reviews of Geophysics*, 54(3), 523–610. <https://doi.org/10.1002/2015rg000510>
- Dakos, V., Carpenter, S. R., Brock, W. A., Ellison, A. M., Guttal, V., Ives, A. R., et al. (2012). Methods for detecting early warnings of critical transitions in time series illustrated using simulated ecological data. *PLoS One*, 7(7), e41010. <https://doi.org/10.1371/journal.pone.0041010>
- Dakos, V., Scheffer, M., Van Nes, E. H., Brovkin, V., Petoukhov, V., & Held, H. (2008). Slowing down as an early warning signal for abrupt climate change. *Proceedings of the National Academy of Sciences*, 105(38), 14308–14312. <https://doi.org/10.1073/pnas.0802430105>
- De Jong, R., Verbesselt, J., Schaepman, M. E., & De Bruin, S. (2012). Trend changes in global greening and browning: Contribution of short-term trends to longer-term change. *Global Change Biology*, 18(2), 642–655. <https://doi.org/10.1111/j.1365-2486.2011.02578.x>
- Dijkstra, H. A. (2013). *Nonlinear climate dynamics*. Cambridge University Press.
- Doughty, C. E., Keany, J. M., Wiebe, B. C., Rey-Sanchez, C., Carter, K. R., Middleby, K. B., et al. (2023). Tropical forests are approaching critical temperature thresholds. *Nature*, 621(7977), 105–111. <https://doi.org/10.1038/s41586-023-06391-z>
- Engelmark, O. (1999). Boreal forest disturbances. In *Ecosystems of the world* (pp. 161–186).
- Forzieri, G., Girardello, M., Ceccherini, G., Spinoni, J., Feyen, L., Hartmann, H., et al. (2021). Emergent vulnerability to climate-driven disturbances in European forests. *Nature Communications*, 12(1), 1081. <https://doi.org/10.1038/s41467-021-21399-7>
- Frankenberg, C., Fisher, J. B., Worden, J., Badgley, G., Saatchi, S. S., Lee, J.-E., et al. (2011). New global observations of the terrestrial carbon cycle from GOSAT: Patterns of plant fluorescence with gross primary productivity. *Geophysical Research Letters*, 38(17), L17706. <https://doi.org/10.1029/2011gl048738>
- Friedl, M., & Sulla-Menashe, D. (2022). MODIS/Terra+ aqua land cover type yearly L3 global 0.05 Deg CMG V061 [Dataset]. *NASA EOSDIS Land Processes Distributed Active Archive Center*. <https://doi.org/10.5067/modis/mcd12c1.061>
- García-Palacios, P., Gross, N., Gaitán, J., & Maestre, F. T. (2018). Climate mediates the biodiversity–ecosystem stability relationship globally. *Proceedings of the National Academy of Sciences*, 115(33), 8400–8405. <https://doi.org/10.1073/pnas.1800425115>
- Gardiner, C. W., (1985). Handbook of stochastic methods for physics, chemistry and the natural sciences. In *Springer series in synergetics*.

- Gatti, L. V., Basso, L. S., Miller, J. B., Gloor, M., Gatti Domingues, L., Cassol, H. L., et al. (2021). Amazonia as a carbon source linked to deforestation and climate change. *Nature*, 595(7867), 388–393. <https://doi.org/10.1038/s41586-021-03629-6>
- Guo, M., Li, J., Yu, F., Yin, S., Huang, S., & Wen, L. (2021). Estimation of post-fire vegetation recovery in boreal forests using solar-induced chlorophyll fluorescence (SIF) data. *International Journal of Wildland Fire*, 30(5), 365–377. <https://doi.org/10.1071/wf20162>
- Han, Y., Qu, Y., Jiang, T., Zhang, X., Lyu, J., & Su, X. (2025). Ecosystems resilience assessment of forest and grassland subjected to ecological drought. *Ecological Indicators*, 173, 113437. <https://doi.org/10.1016/j.ecolind.2025.113437>
- Harris, I., Osborn, T. J., Jones, P., & Lister, D. (2020). Version 4 of the CRU TS monthly high-resolution gridded multivariate climate dataset [Dataset]. *Scientific Data*, 7(1), 109. <https://doi.org/10.1038/s41597-020-0453-3>
- Hirota, M., Holmgren, M., Van Nes, E. H., & Scheffer, M. (2011). Global resilience of tropical forest and savanna to critical transitions. *Science*, 334(6053), 232–235. <https://doi.org/10.1126/science.1210657>
- Johnstone, J. F., Allen, C. D., Franklin, J. F., Frelich, L. E., Harvey, B. J., Higuera, P. E., et al. (2016). Changing disturbance regimes, ecological memory, and forest resilience. *Frontiers in Ecology and the Environment*, 14(7), 369–378. <https://doi.org/10.1002/fee.1311>
- Jones, T. S., Logan, B. A., Reblin, J. S., Bombard, D. M., Ross, B. P., Allen, D. W., et al. (2023). Stress-induced changes in photosynthesis and proximal fluorescence emission of turfgrass. *Environmental Research Communications*, 5(11), 111005. <https://doi.org/10.1088/2515-7620/ad0b29>
- Kendall, M. G. (1948). Rank correlation methods.
- Kim, J. E., Wang, J. A., Li, Y., Czimeczik, C. I., & Randerson, J. T. (2024). Wildfire-induced increases in photosynthesis in boreal forest ecosystems of North America. *Global Change Biology*, 30(1), e17151. <https://doi.org/10.1111/gcb.17151>
- Koppen, W. (1936). Das geographische System de Klimate. In *Handbuch der Klimatologie*.
- Lawlor, D. W., & Cornic, G. (2002). Photosynthetic carbon assimilation and associated metabolism in relation to water deficits in higher plants. *Plant, Cell and Environment*, 25(2), 275–294. <https://doi.org/10.1046/j.0016-8025.2001.00814.x>
- Lewis, S. L., Brando, P. M., Phillips, O. L., Van Der Heijden, G. M., & Nepstad, D. (2011). The 2010 Amazon drought. *Science*, 331(6017), 554–554. <https://doi.org/10.1126/science.1200807>
- Li, B., Beaudoin, H., & Rodell, M. (2018). NASA/GSFC/HSL, GLDAS Catchment Land Surface Model L4 Daily 0.25x 0.25 degree V2. 0 [Dataset]. *Goddard Earth Sciences Data and Information Services Center (GES DISC)*. <https://doi.org/10.5067/lyha9088mfqw>
- Marrs, J., Reblin, J., Logan, B., Allen, D., Reinmann, A., Bombard, D., et al. (2020). Solar-induced fluorescence does not track photosynthetic carbon assimilation following induced stomatal closure. *Geophysical Research Letters*, 47(15), e2020GL087956. <https://doi.org/10.1029/2020gl087956>
- Mohammadi, K., Jiang, Y., & Wang, G. (2022). Flash drought early warning based on the trajectory of solar-induced chlorophyll fluorescence. *Proceedings of the national academy of Sciences*, 119(32), e2202767119. <https://doi.org/10.1073/pnas.2202767119>
- Oliver, T. H., Heard, M. S., Isaac, N. J., Roy, D. B., Procter, D., Eigenbrod, F., et al. (2015). Biodiversity and resilience of ecosystem functions. *Trends in Ecology & Evolution*, 30(11), 673–684. <https://doi.org/10.1016/j.tree.2015.08.009>
- Peel, M. C., Finlayson, B. L., & McMahon, T. A. (2007). Updated world map of the Köppen-Geiger climate classification. *Hydrology and Earth System Sciences*, 11(5), 1633–1644. <https://doi.org/10.5194/hess-11-1633-2007>
- Pettorelli, N., Vik, J. O., Mysterud, A., Gaillard, J.-M., Tucker, C. J., & Stenseth, N. C. (2005). Using the satellite-derived NDVI to assess ecological responses to environmental change. *Trends in Ecology & Evolution*, 20(9), 503–510. <https://doi.org/10.1016/j.tree.2005.05.011>
- Phillips, O. L., Aragão, L. E., Lewis, S. L., Fisher, J. B., Lloyd, J., López-González, G., et al. (2009). Drought sensitivity of the Amazon rainforest. *Science*, 323(5919), 1344–1347. <https://doi.org/10.1126/science.1164033>
- Rodell, M., Houser, P., Jambor, U., Gottschalck, J., Mitchell, K., Meng, C.-J., et al. (2004). The global land data assimilation system. *Bulletin of the American Meteorological Society*, 85(3), 381–394. <https://doi.org/10.1175/bams-85-3-381>
- Scheffer, M., Bascompte, J., Brock, W. A., Brovkin, V., Carpenter, S. R., Dakos, V., et al. (2009). Early-warning signals for critical transitions. *Nature*, 461(7260), 53–59. <https://doi.org/10.1038/nature08227>
- Seddon, A. W., Macias-Fauria, M., Long, P. R., Benz, D., & Willis, K. J. (2016). Sensitivity of global terrestrial ecosystems to climate variability. *Nature*, 531(7593), 229–232. <https://doi.org/10.1038/nature16986>
- Smith, T., & Boers, N. (2023a). Global vegetation resilience linked to water availability and variability. *Nature Communications*, 14(1), 498. <https://doi.org/10.1038/s41467-023-36207-7>
- Smith, T., & Boers, N. (2023b). Reliability of vegetation resilience estimates depends on biomass density. *Nature Ecology & Evolution*, 7(11), 1799–1808. <https://doi.org/10.1038/s41559-023-02194-7>
- Smith, T., Traxl, D., & Boers, N. (2022). Empirical evidence for recent global shifts in vegetation resilience. *Nature Climate Change*, 12(5), 477–484. <https://doi.org/10.1038/s41558-022-01352-2>
- Sun, Y., Frankenberg, C., Wood, J. D., Schimel, D., Jung, M., Guanter, L., et al. (2017). OCO-2 advances photosynthesis observation from space via solar-induced chlorophyll fluorescence. *Science*, 358(6360), eaam5747. <https://doi.org/10.1126/science.aam5747>
- Wang, M., Fan, L., Frappart, F., Ciais, P., Sun, R., Liu, Y., et al. (2021). An alternative AMSR2 vegetation optical depth for monitoring vegetation at large scales. *Remote Sensing of Environment*, 263, 112556. <https://doi.org/10.1016/j.rse.2021.112556>
- Woodgate, W., Phinn, S., Devereux, T., & Aryal, R. R. (2025). Bushfire recovery at a long-term tall eucalypt flux site through the lens of a satellite: Combining multi-scale data for structural-functional insight. *Remote Sensing of Environment*, 317, 114530. <https://doi.org/10.1016/j.rse.2024.114530>
- Zarco-Tejada, P. J., Morales, A., Testi, L., & Villalobos, F. J. (2013). Spatio-temporal patterns of chlorophyll fluorescence and physiological and structural indices acquired from hyperspectral imagery as compared with carbon fluxes measured with eddy covariance. *Remote Sensing of Environment*, 133, 102–115. <https://doi.org/10.1016/j.rse.2013.02.003>
- Zhang, Y., Joiner, J., Alemohammad, S. H., Zhou, S., & Gentine, P. (2018). A global spatially contiguous solar-induced fluorescence (CSIF) dataset using neural networks [Dataset]. *Biogeosciences*, 15(19), 5779–5800. <https://doi.org/10.5194/bg-15-5779-2018>
- Zhang, Y., Wang, J. A., Berner, L. T., Goetz, S. J., Zhao, K., & Liu, Y. (2024). Warming and disturbances affect arctic-boreal vegetation resilience across northwestern North America. *Nature Ecology & Evolution*, 8(12), 2265–2276. <https://doi.org/10.1038/s41559-024-02551-0>